Peer-reviewed version available at *Nanomaterials* **2019**, *9*, 1372; doi:10.3390/nano9101372

Article

Dysprosium removal from water using active carbons obtained from spent coffee ground

L. Alcaraz [1], M.E. Escudero [1], F.J. Alguacil [1], I. LLorente [1], A. Urbieta [2], P. Fernandez [2], and F.A. López [1,*]

[1] National Center for Metallurgical Research (CENIM). Spanish National Research Council (CSIC). Avda. Gregorio del Amo, 8. 28040, Madrid, Spain
[2] Department of Materials Physics, Faculty of Physics, Complutense University of Madrid, Madrid, Spain
* Correspondence: f.lopez@csic.es

Abstract: This paper describes the physico-chemical study of the adsorption of dysprosium (Dy^{3+}) in aqueous solution onto two types of activated carbons synthesized from spent coffee ground. KOH activated carbon is a microporous material with a specific BET surface area of 2330 $m^2 \cdot g^{-1}$ and pores with a diameter of 3.2 nm. Carbon activated with water vapor and N_2 is a solid mesoporous, with pores of 5.7 nm in diameter and a specific surface of 982 $m^2 \cdot g^{-1}$. A significant dependence of the adsorption capacity on the solution pH was found, while it does not depend significantly neither on the dysprosium concentration nor on the temperature. A maximum adsorption capacity of 31.26 $mg \cdot g^{-1}$ and 33.52 $mg \cdot g^{-1}$ for the chemically and physically activated carbons, respectively, were found. In both cases, the results obtained from adsorption isotherms and kinetic study were better fit to a Langmuir model and a pseudo-second-order kinetics. In addition, thermodynamic results indicate that dysprosium adsorption onto both activated carbons is an exothermic, spontaneous and favorable process.

Keywords: dysprosium; activated carbon, spent coffee ground, adsorption

1. Introduction

Nowadays, rare earths (REE) are becoming increasingly interesting due to their essential role in several applications such as permanent magnets, phosphor lamps, rechargeable NiMH batteries or catalysts, among others [1]. The increasing popularity of hybrid and electric cars, wind turbines and/or compact fluorescent lamps is causing an increase in the demand and price of REEs since several compounds of REE such as neodymium, dysprosium, and others [2] are in smart-batteries that power every electric and hybrid-electric vehicle [3]. Since 2010, the European Commission in the report Critical Raw Materials for the European Union considers the REE as the most critical raw materials group. Among them, neodymium (Nd), europium (Eu), terbium (Tb), dysprosium (Dy) and yttrium (Y) are the five most critical REE [1]. It is expected that the demand for Nd and Dy will rise by 700% and 2600% over the next 25 years, respectively [4].

On the other hand, the technological development has increased the dumping of electronic waste which is facilitating the release of significant quantities of these elements along with several other toxic elements in to the subsoils and groundwater [3], hence the investigation on the different adsorption process is fully pertinent. To the best of our knowledge, maximum acceptable limits for REE in drinking water are not available from any international health organization, neither sufficient data about their toxicity to human health. However, contamination of the environment by different kinds of toxic species is one of the most serious problems today. Thus, the REE group represents important elements found in the environment and need to be studied at greater depth to understand their effects on human health, and the removal or recovery options from the environment should be deeply investigated [3].

Among the different methods to eliminate contaminants, adsorption onto different carbonaceous materials is an efficient option because of its simplicity and cost effectiveness [5,6].

Nowadays, the most commonly adopted adsorbent, for instance to remove pollutants from water, is the activated carbon, which are characterized by its highly porosity, great surface area and high degree of surface reactivity [7]. In this sense, the obtention of activated carbons from renewable and cheaper precursors is catching increasing attention from the researchers [7]. Several investigations have been developed about the use of biomass as a precursor, such as residues derived from tea [8,9], coffee [10,11], winemaking waste [12,13] and olives bones [14,15] in order to obtain activated carbon.

In the present work, we obtained activated carbons from spent coffee waste. These activated carbons were both physically and chemically activated. Characterization of both activated carbons and their capacity of dysprosium adsorption were assessed.

2. Materials and Methods

2.1. Synthesis of the activated carbons

Coffee waste recovered from the beverage preparation (spent coffee ground, SCG) were provided by the commercial canteen. Coffee ground used was a mixture 10 (wt,%) roasted and 90 (wt,%) natural.

SCG were subjected to a hydro-alcoholic process in an extraction medium (EtOH:H_2O, v/v) 50:50 at 393 K for 30 min in order to obtain the corresponding precursor. Finally, the precursor obtained was turned into activated carbon by both chemical and physical processes.

Chemical activation

To perform the chemical activation 1 g of the precursor was mixed with 1.5 g of the KOH. The homogenized mixtures were placed in alumina crucibles and treated in a Carbolite STF 15 tubular oven at 1123 K for 30 min under a nitrogen carrier (150 mL·min^{-1}). After cooling down to room temperature, the black solid obtained was washed several times with Milli-Q water until neutral pH was achieved. The obtained sample is named as AC-CA.

Physical activation

The physical activation of the precursor was carried out in a quartz reactor at 1073 K for 120 min. Approximately 20 g of precursor was added into the reactor. N_2 with a flow rate of 0.5 mL·min^{-1} was pumped into the reactor throughout the activation to act as gas carrier during the heating ramp. When the treatment temperature was achieved, deionized water is introduced in the reactor by means of a peristaltic pump, with a similar flow rate, hence changing from N_2 to The obtained sample is named as AC-PA.

2.2. Characterization of the activated carbons

The porous structure of the activated carbons was characterized by N_2 adsorption at 77 K using an Accelerated Surface Area and Porosimetry System (Micromeritics ASAP 2020). The samples were partially degassed at 623 K for 16 h. The specific surface was determined by analyzing the adsorption isotherm via the BET (Brunauer–Emmett–Teller) equation and Density Functional Theory (DFT) models, employing Micromeritics and Quantachrome software.

The surface of the activated carbons was examined by field emission scanning electron microscope (FE-SEM) using a Hitachi S 4800 J microscope.

2.3. Adsorption experiments

Dysprosium adsorption by both activated carbons (AC-CA and AC-PA) was carried out via batch experiments. For it, stock solution of dysprosium (1000 mg·L^{-1}) were prepared by dissolving $Dy(NO_3)_3 \cdot xH_2O$ (Sigma Aldrich) in MilliQ water. Then, stock solution was diluted to obtain the different concentrations. The temperature was controlled using a Selecta Termotronic thermostat bath equipped with multiple Lab Companion MS-52M stirrers. Aliquots (1 mL) of the solution were extracted every 15 minutes and filtered through a syringe filters with a 0.22 μm pore and 13 mm diameter. The pH of the solutions was adjusted with HCl (0.1 M) until the desirable value was

achieved. Dysprosium content in the solution was analyzed by coupled plasma optical emission spectrometry (ICP-OES) using an Agilent 5100.

The dysprosium adsorbed percentage and the adsorption capacity at each time t (q_t ($mg \cdot g^{-1}$)) were calculated by the following equations:

$$Adsorbed\ Dy = \frac{(c_0 - c_e)}{c_0} \cdot 100 \quad (1)$$

$$q_t = \frac{(C_0 - C_e) \cdot V}{m} \quad (2)$$

The equilibrium adsorption isotherm data were plotted using the linear forms of Langmuir (equation 3), Freundlich (equation 4), and Temkin (equation 5) models [16]:

$$\text{Langmuir:} \quad \frac{C_e}{q_e} = \frac{1}{q_m \cdot b} + \frac{1}{q_m} \cdot c_e \quad (3)$$

$$\text{Freundlich:} \quad \ln q_e = \ln K_F + \frac{1}{n} \cdot \ln C_e \quad (4)$$

$$\text{Temkin:} \quad q_e = B \cdot \ln A_T + B \cdot \ln c_e \quad (5)$$

Kinetics experiments were analyzed using the pseudo-first-order (equation 6) and pseudo-second-order (equation 7) models, and were carried out at different temperatures:

$$\text{pseudo-first order:} \quad \ln(q_e - q_t) = \ln q_e - K_1 \cdot t \quad (6) \quad [17]$$

$$\text{pseudo-second order:} \quad \frac{t}{q_t} = \frac{1}{K_2 \cdot q_e^2} + \frac{1}{q_e} \cdot t \quad (7) \quad [18]$$

Activation energy (E_a) can be calculated from the Arrhenius equation (equation 8) expressed as:

$$k_2 = A \cdot e^{(-E_a/R \cdot T)} \quad (8)$$

Enthalpy change (ΔH^0) and entropy change (ΔS^0) were calculated from the slope and intercept of a plot of log (q_e/c_e) versus 1/T [19] using the equations (equation 9) and (equation 10):

$$\log \frac{q_e}{c_e} = \frac{\Delta S^0}{2.303R} + \frac{\Delta H^0}{2.303RT} \quad (9)$$

$$\Delta G^0 = \Delta H^0 - T\Delta S^0 \quad (10)$$

μ-Photoluminescence (μ-PL) and Raman experiments were performed at room temperature in a Horiba Jovin Yvon LabRAM HR800 confocal microscope. A He-Cd laser (λ_{ex}=325 nm) was used as excitation source for PL while Raman spectra were recorded under excitation at 632.8 nm line of a He-Ne laser. A charge coupled device (CCD) detector was used to collect the scattered light dispersed by a 600 lines·mm^{-1} grating. The spectral resolution of the system used was 1.5 cm^{-1} for micro-Raman measurements and 0.1 nm for PL measurements.

A VG Microtech model MT500 spectrophotometer with a non-monochromatic MgK_α1.2 X-Ray source operating at 300W was used. The XPS analysis chamber pressure was maintained below 10^{-8} torr during data acquisition. Calibration of the energy scale was performed with an Ag $3d^{5/2}$ (368.3 eV) standard. The peaks were fitted using a Gaussian-Lorentzian mixed function, after a Shirley background subtraction. C1s sp^2 at 284.5 eV was used as binding energy (BE) reference.

3. Results and discussion

Preprints (www.preprints.org) | NOT PEER-REVIEWED | Posted: 6 August 2019 doi:10.20944/preprints201908.0076.v1

Peer-reviewed version available at Nanomaterials 2019, 9, 1372; doi:10.3390/nano9101372

3.1. Characterization of the activated carbons

3.1.1. Textural properties

The pore volume, pore size and the total specific surface area on AC-CA and AC-PA activated carbons were determined by the BET technique. The AC-CA with a basically microporous structure were obtained, as can be appreciated in Table 1, with the total pore volume (V_P) very similar to the volume of micropores (W_0) a pores diameter (D_P) of <3.29 nm (micropores). The BET surface area is 2330 $m^2 \cdot g^{-1}$. In the AC-PA the volume of micropores is much lower than the total pore volume, which indicate that it is a mesoporous material, with pores of 4.8 mm. The non-microporous surface is much larger that the microporous surface, in accordance with the previous data. The specific BET surface is 981 $m^2 \cdot g^{-1}$.

Texturally, both activated carbons are very different and consequently they should have different behavior in the Dy adsorption process.

The N_2 adsorption isotherm of AC-CA (Fig. 1a) is of type I, according to the IUPAC classification [20]. This isotherm is characteristic of microporous solids. Fig. 1b shows the pore size distribution (BJH desorption). The average pore diameter is 3.29 nm. In the case of AC-PA, the adsorption isotherm (Fig. 1c) is of type IV, characteristics of solid that present aggregates of particles in the form of slit-shaped. The pore size distribution (Fig. 1d) shows an average pore diameter of 5.68 nm.

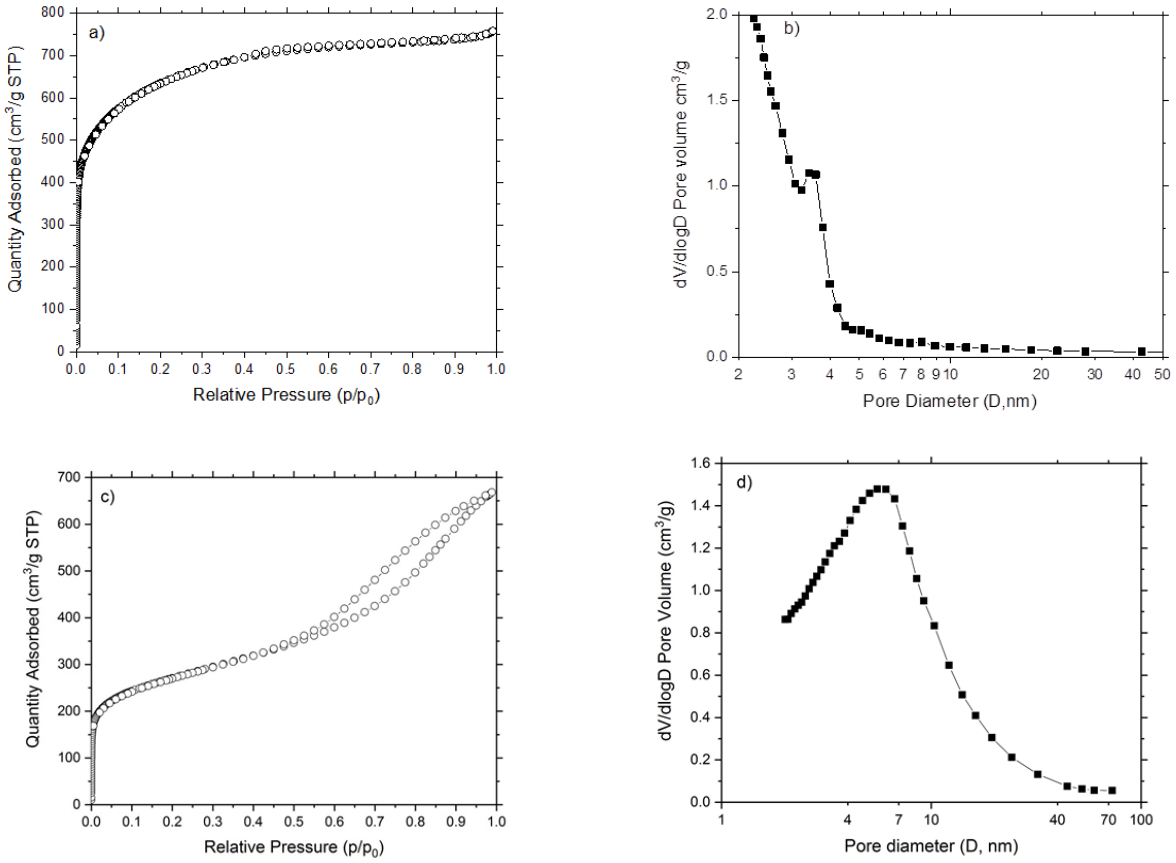

Figure 1. Adsorption isotherms and pore size distributions of (**a/b**) AC-CA and (**c/d**) AC-PA.

Table 1. Textural characterization of the activated carbons.

Sample	V_T ($cm^3 \cdot g^{-1}$)	$V_{\mu p}$ ($cm^3 \cdot g^{-1}$)	D_P (nm)	$S_{\mu s}$ ($m^2 \cdot g^{-1}$)	$NS_{\mu s}$ ($m^2 \cdot g^{-1}$)	S_{BET} ($m^2 \cdot g^{-1}$)
AC-QA	1.17	1.07	3.29	2265.0	65.6	2330.6
AC-PA	1.03	0.03	5.68	244.8	736.8	981.6

Peer-reviewed version available at Nanomaterials 2019, 9, 1372; doi:10.3390/nano9101372

3.1.2. Scanning electron microscopy (SEM)

The surface characteristics of the activated carbons were analyzed using SEM technique. Different morphologies can be clearly observed. The chemically activated carbon (Fig. 2a) show homogeneous surface morphology with a large number of pores, caused by the chemical interaction between KOH and the precursor surface. On the other hand, AC-PA (Fig. 2b) exhibit a surface less porous than in the case described above, with a pitted and cracked surface typical of the physically activated carbons [21].

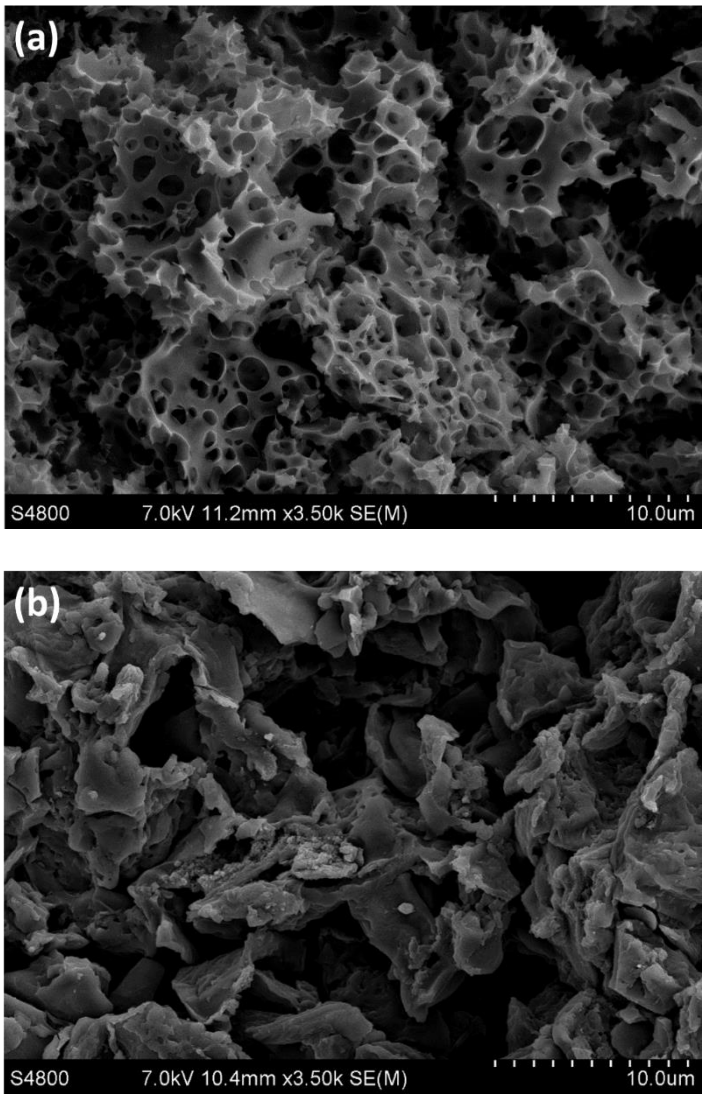

Figure 2. SEM micrographs of (**a**) AC-CA and (**b**) AC-PA samples.

3.1.3. Raman spectroscopy

Characterization of both active carbons was carried out by Raman spectroscopy. It is a useful technique for carbon materials, because of the spectral shape drastically changes not only due to the kind of abundant allotropic forms of carbon, but to the fine structural changes of the individual allotrope [22]. In this sense, polycrystalline graphites exhibit two sharp peaks: G-band (at around 1580 cm^{-1}) and D-band (at around 1355 cm^{-1}. These bands are generally attributed to E_{2g} and A_{1g} in-plane vibration modes respectively and the graphitization degree of a carbon material is generally characterized by the I_G/I_D value in the Raman spectra. Both vibration modes are represented schematically in Fig. 3. In part a of the scheme, the breathing mode A_{1g} (D band) is shown, and part

b illustrates the vibration mode E_{2g} (G band) [23,24]. On the other hand, in amorphous carbon a broad bands around 1550 cm^{-1} overlapped with a broader band around 1400 cm^{-1} is observed [22,25].

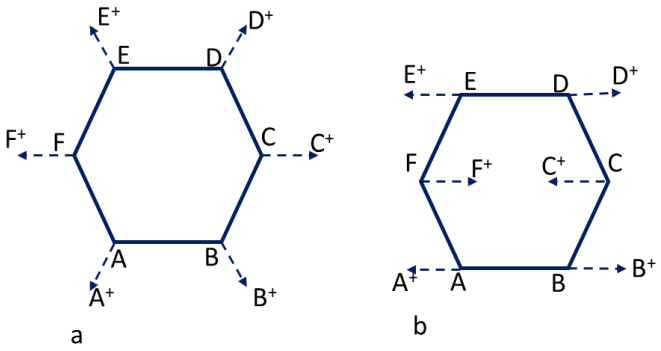

Figure 3. Scheme of the vibration modes: (**a**) Breathing mode A_{1g} (D peak) and (**b**) Vibration mode E_{2g} (G peak).

Comparative normalized spectra of AC-CA and AC-PA activated carbons are shown in Fig. 4. Both samples exhibit two Raman bands peaked at 1595 cm^{-1} and 1334 cm^{-1}. A broadening of the Raman bands can be appreciated in AC-CA sample in comparison to the AC-PA sample. In addition, the Raman band centered at 1334 cm^{-1} exhibit the higher intensity in both cases. This effect is more noticeable in the AC-PA activated carbon spectrum.

In the present case, the I_G/I_D (AC-PA) > I_G/I_D (AC-CA) which indicate the highest graphitization degree of the AC-PA activated carbon sample. Previous investigations carried out with carbon nanomaterials reported that the adsorption capacity are related with the graphitization degree [24].

3.2. Adsorption experiments

We have studied the influence of three different parameters on the adsorption capacity of both types of activated carbons: solution pH, Dy concentration and activated carbon amount.

3.2.1. Influence of the solution pH

In order to analyze the influence of the solution pH on the adsorption process, experiments were carried out at three different pH values (3 to 5). For this purpose, 30 mg of the activated carbons were added to 200 mL solution containing 5 $mg{\cdot}L^{-1}$ of Dy ions. The adsorbed dysprosium amounts versus the contact time at different pH values for both types of AC are plotted in Fig. 5.

In both cases (AC-CA and AC-PA), the adsorption capacity increases when the pH increases from 3 to 4 and then decreases. As previously reported [26], dysprosium may be present in the solution either as an isolated cation (Dy^{+3}) or as hydroxide cation ($Dy(OH)^{2+}$), consequently the behavior in aqueous solution is a complex phenomenon. According to Qaader et al. [26] at a pH between 1 and 4 the predominant species is Dy^{3+}, while at higher pH values Dy^{3+} ions start to get hydrolyzed leading to the formation of other species, such as $Dy(OH)^{2+}$.

Preprints (www.preprints.org) | NOT PEER-REVIEWED | Posted: 6 August 2019 doi:10.20944/preprints201908.0076.v1

Peer-reviewed version available at Nanomaterials 2019, 9, 1372; doi:10.3390/nano9101372

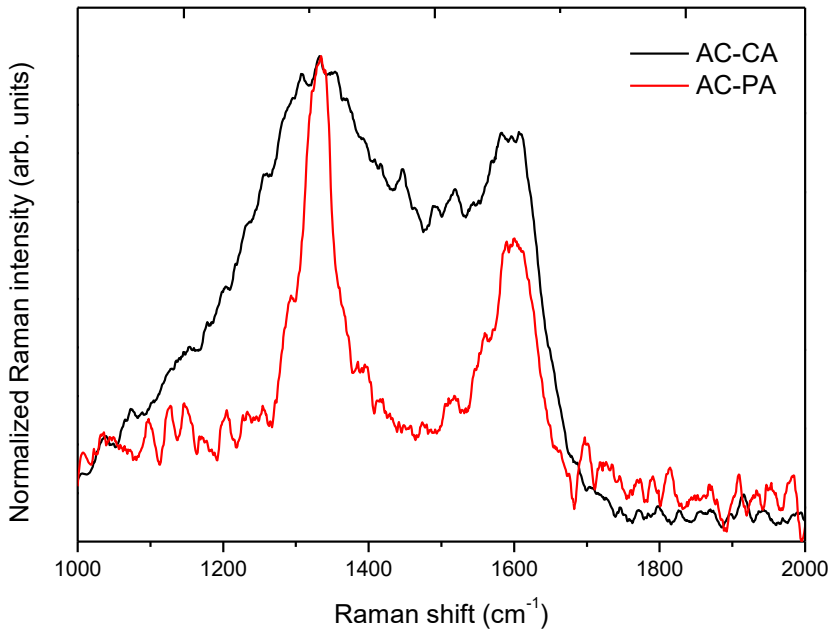

Figure 4. Normalized Raman spectra of both activated carbons.

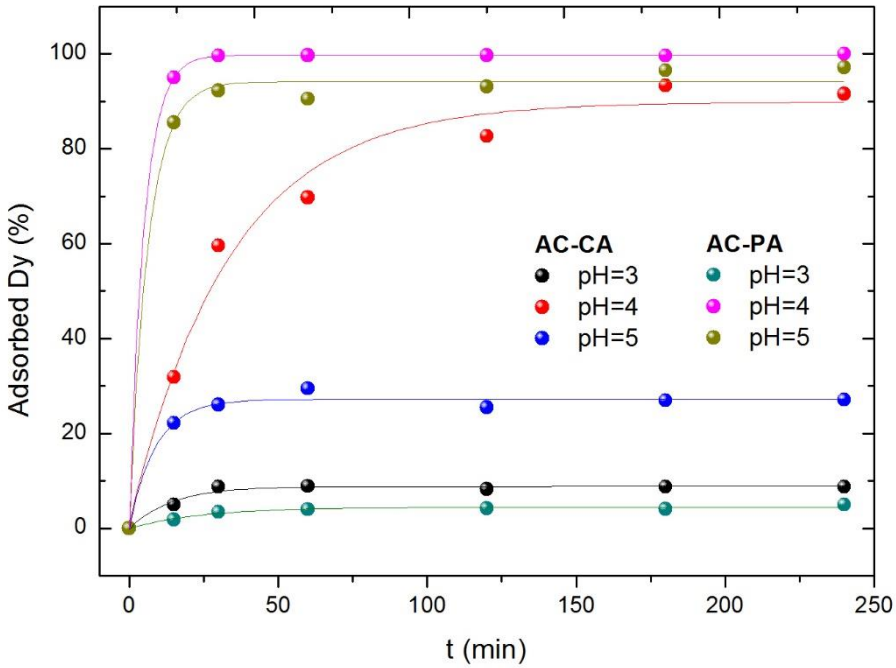

Figure 5. Effect of the solution pH for AC-CA and AC-PA.

These species are weakly adsorbed as compared to Dy^{3+} ions; therefore, the adsorption of dysprosium starts to decrease above pH 5, and the highest adsorption was found at value of pH of 4,

obtaining a maximum adsorption percentage of 94 % for AC-CA and practically 100 % for AC-PA. The adsorption capacity of AC-PA was higher than AC-CA for all pH values investigated.

3.2.2. Influence of the dysprosium concentration

The influence of dysprosium concentration has been studied with three solutions with Dy concentrations of 2.5, 5 and 10 mg/L, and a fixed amount of activated carbon, 30 mg. All the experiments were carried out at room temperature. The results are shown in Fig. 6.

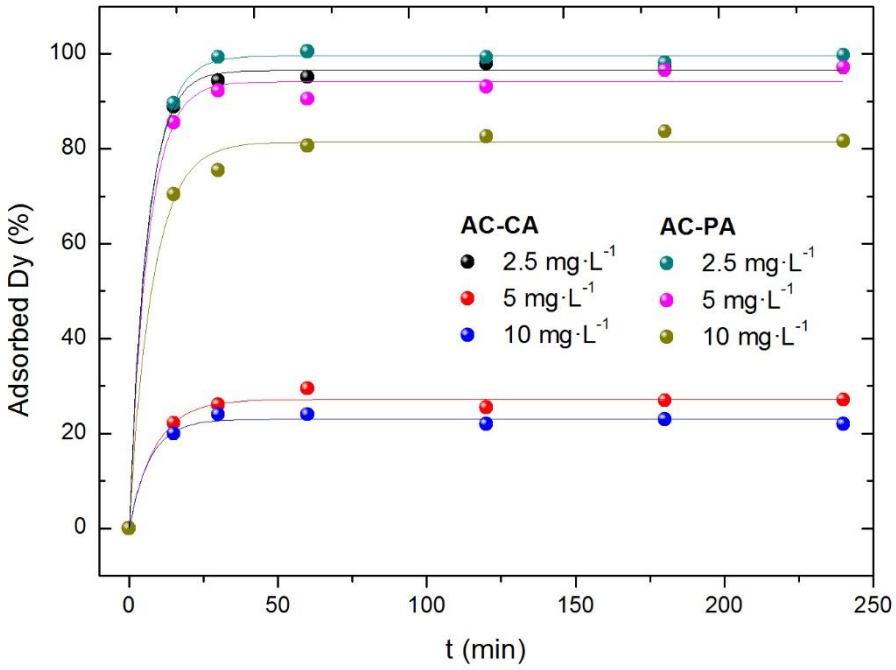

Figure 6. Effect of the dysprosium concentration in the adsorption percentage.

In both cases (AC-CA and AC-PA), the adsorbed Dy percentage decreases with increasing RE concentration. In the case of AC-PA, the adsorption percentages are quite high, ranging from 99% for the lowest Dy concentration to 80% for the largest. However, the AC-CA samples show lower adsorption percentages. In fact, only for the solution with the lowest Dy concentration a significant adsorption, 96%, is obtained (similar to that of AC-PA). For the solutions with 5 and 10 mg·L^{-1} of Dy much lower adsorption capacities are observed, between 20 and 30%).

3.2.3. Influence of the activated carbon amount

Finally, the influence of the adsorbent amount has been studied. Solutions of Dy with 5 mg·L^{-1} of concentration were put in contact with different amounts of both ACs (5, 15, 30 and 60 mg). The results are plotted in Fig. 7.

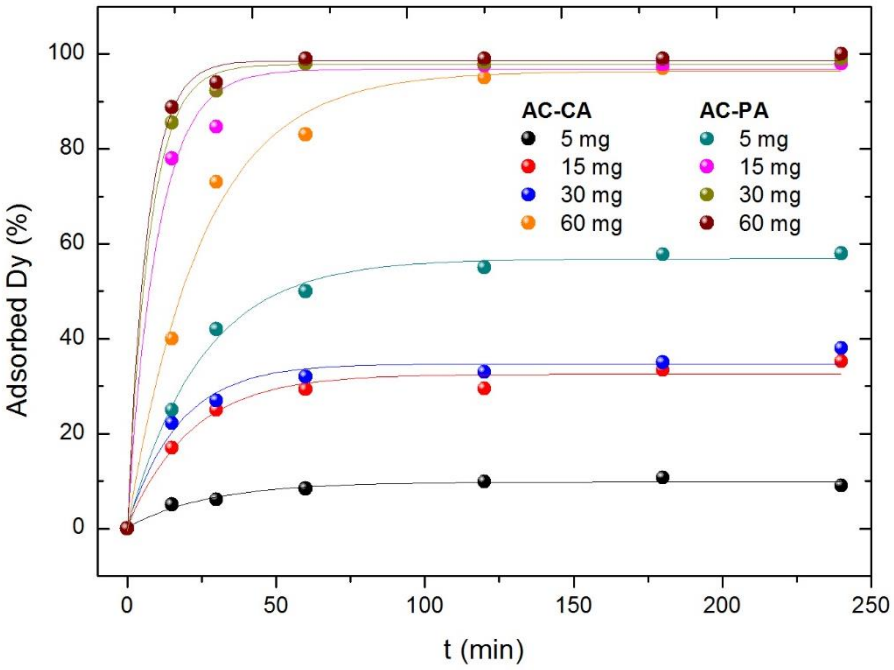

Figure 7. Variation of the adsorption percentage with the adsorbent amount.

As for the other parameters, the best results are obtained for the AC-PA. As expected, the larger the amount of adsorbent, the larger the adsorption percentage, however the behavior of the two kind of samples is significantly different. In the case of the AC-PA, the adsorption percentage increases drastically (from 57% to 99%) when the AC amount increases from 5 mg to 15 mg, then, it remains practically constant with the amount of adsorbent. However, in the case of the AC-CA, the adsorption depends strongly on the adsorbent amount, going from 10% (5 mg of the AC) to 96% (60 mg of the AC). Only for the largest adsorbent amount the adsorption percentage is comparable to those of AC-PA, and even in this case, the time required to reach a similar adsorption percentage is much longer. Only for the largest adsorbent amount (60 mg) and times around 120 min comparable adsorption values are reached.

3.2.4. Equilibrium isotherms

As observed from the adsorption results previously shown (Figs. 4 to 6) the equilibrium adsorption percentage is reached after a period of time ranging from approximately 50 to 120 minutes depending on the experiment conditions. For the sake of the kinetic study we will adopt as equilibrium values those obtained at 120 minutes, since at this time the equilibrium has been achieved in all the experimental conditions.

Equilibrium isotherms were measured modifying the adsorbent amount and using equations 3 to 5. In Table 2 the calculated parameters and the corresponding correlation coefficients are shown. For both ACs, the best correlation is obtained with the Langmuir model. According to this model, the maximum adsorption capacity values (q_m) calculated were 28.11 $mg \cdot g^{-1}$ and 29.05 $mg \cdot g^{-1}$ for AC-CA and AC-PA, respectively. These results are similar to those obtained experimentally (31.26 $mg \cdot g^{-1}$ and 33.52 $mg \cdot g^{-1}$). As expected, according to the results previously discussed, the AC-PA showed the greatest adsorption capacity. The values calculated for Langmuir non-dimensional factors (RL) are 0.02 and 0.03 for AC-CA and AC-PA respectively, which indicates that the dysprosium adsorption is a favorable process.

Preprints (www.preprints.org) | NOT PEER-REVIEWED | Posted: 6 August 2019 doi:10.20944/preprints201908.0076.v1

Peer-reviewed version available at Nanomaterials 2019, 9, 1372; doi:10.3390/nano9101372

Table 2. Calculated isotherm parameters for the Langmuir, Freundlich and Temkin linear models.

Sample	Langmuir				Freundlich			Temkin		
	q_m (mg·g^{-1})	b (L·mg^{-1})	R_L	R^2	K_F (L·g^{-1})	1/n	R^2	A_T	b_T	R^2
AC-CA	28.11	6.42	0.02	0.996	24.82	0.08	0.713	0.23	0.16	0.582
AC-PA	29.05	10.5	0.03	0.998	81.44	0.17	0.722	0.79	0.10	0.800

3.2.5. Effect of the temperature, kinetic and thermodynamic study

Experiments at different three temperatures (303, 318 and 333 K) were carried out to evaluate the influence of temperature on adsorption process. For this experiment, 30 mg of the AC were put in contact with a Dy dissolution with a concentration of 5 mg·L^{-1}. As can be appreciated in Fig. 8, the behavior of both types of samples is considerably different. In the AC-PA samples, temperature does not seem to play a significant role (within the temperature interval under consideration). For all temperatures investigated, the equilibrium value is reached after a relatively short time, around 25 minutes. In the case of the AC-CA sample, at the lowest temperature, a very low adsorption degree is reached, 27%. At 318 K the adsorption percentage is closer to that obtained for AC-PA samples, and at 333 K similar values are obtained for both types of activated carbons.

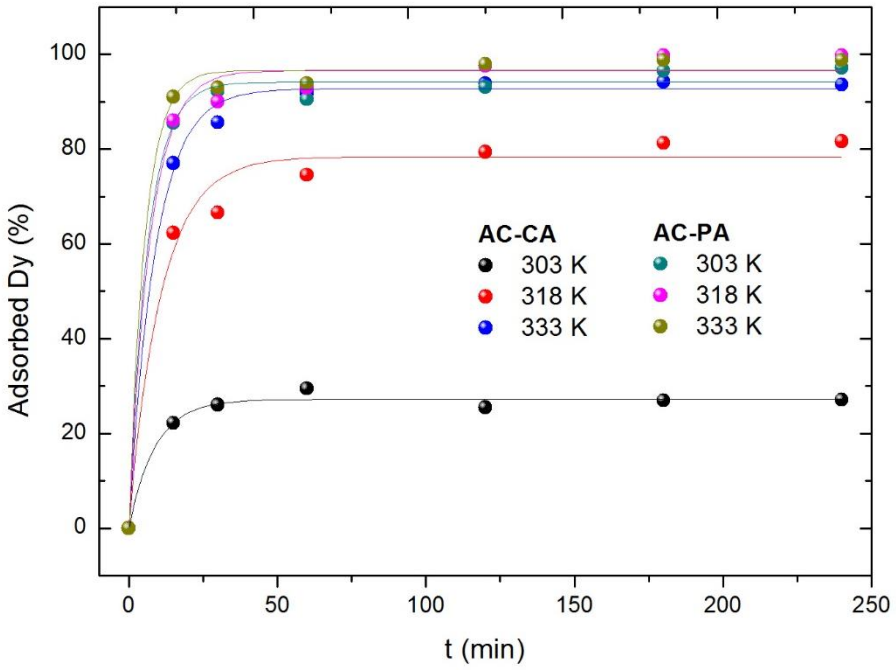

Figure 8. Dysprosium adsorption percentage with the temperature variation.

Adsorption kinetics studies were carried out using the equations 6 and 7. The calculated parameters from the corresponding fits are included in Table 3. For both type of samples, the best fitted results were found for a pseudo-second-order model. With respect to the kinetic reaction constants, k_2 increases as the temperature does which indicates that the temperature favors the adsorption process. In fact, if we consider the k_2 values obtained for AC-CA samples, the influence of temperature seems to be larger than for the AC-PA samples, in agreement with the results described from Fig. 8.

Preprints (www.preprints.org) | NOT PEER-REVIEWED | Posted: 6 August 2019 doi:10.20944/preprints201908.0076.v1

Peer-reviewed version available at Nanomaterials 2019, 9, 1372; doi:10.3390/nano9101372

Table 3. Calculated kinetics parameters at different temperatures.

Sample	T (K)	Pseudo-first-order			Pseudo-second-order		
		k1	qe	R2	k2 (·10-3)	qe	R2
AC-CA	303	0,016	17,693	0,784	0,795	32,362	0,997
	318	0,017	19,470	0.830	1,012	32,467	0,995
	333	0,057	19,931	0,933	1,172	33,670	0,999
AC-PA	303	0,020	8,194	0,740	0,932	28,490	0,999
	318	0,023	8,366	0,965	1,132	30,120	0,999
	333	0,047	21,270	0,785	1,232	32,362	0,999

As explained in section 2.2, activation energy was estimated the Arrhenius plot ln $k_{2,obs}$ versus 1/T. The value of the activation energy will give us information on the character of the adsorption process. For physical adsorption process, the reactions are reversible, the equilibrium are rapidly achieved, and the activation energies are correspondingly low, in the range from 5 to 40 kJ·mol-1. On the contrary, chemical adsorption, involves stronger forces, and hence requires higher activation energies (40 to 800 kJ·mol^{-1}) [27]. In our case, the calculated activation energies were 10,90 kJ·mol^{-1} and 7,83 kJ·mol^{-1} for AC-CA and AC-PA, respectively, suggesting a physi-sorption process.

Table 4 summarizes the thermodynamic parameters calculated from the equations 8-10. The negative values obtained for the enthalpy change indicate that the dysprosium adsorption is an exothermic process in all the samples studied. Moreover, the adsorption process is spontaneous and favorable at the different temperatures studied for both ACs, as indicated by the free energy change [28]. Finally, the value calculated for the entropy change was positive in both cases, indicating that the entropy of the system increased during the adsorption, i.e. as has been mentioned previously it is a spontaneous process. These results described are indicative of the affinity of the ACs towards Dy ions [27]. Besides, the positive values suggest an increase in adsorbate concentration in the solid-liquid interface (an increase in adsorbate concentration onto the solid phase) [29].

Table 4. Calculated thermodynamic kinetics parameters for both ACs.

Sample	T (K)	$-\Delta H^0$ (kJ·mol^{-1})	ΔS^0 (J·mol^{-1}·K^{-1})	$-\Delta G^0$ (kJ·mol^{-1})
AC-CA	303	79,18	327,64	178,45
	318			183,37
	333			188,29
AC-PA	303	159,65	628,29	350,02
	318			359,44
	333			368,87

3.3. X-ray photoelectron spectroscopy (XPS)

The shape of high resolution Dy 4d XPS spectra and its binding energy were carefully analyzed (Fig. 9). The Dy spectra exhibit doublet components due to the electrostatic interactions of the 4d hole and 4f electrons with spin-orbit splitting of $4d^{5/2}$ and $4d^{3/2}$ states. In the case of $Dy(NO_3)_3$ the characteristic doublet peak appears at 154.2 eV for 4d5/2 and 157.4 eV for 4d3/2, which is according to the standard oxidation state of +3 [30]. Binding energy of Dy 4d5/2 for samples AC-PA:Dy and AC-CA:Dy are 155.0 eV and 153.9 eV, respectively. These results confirm that the Dy remains in the state of Dy3+ after treatment but, in the case of the sample AC-CA:Dy, its BE value is very close to the obtained for $Dy(NO_3)_3$ standard which means that there is no significant difference in the chemistry of Dy in both samples. However, in the case of AC-PA:Dy there is a significant shift to higher binding energies. This could suggest a higher interaction between Dy and C after this treatment. The obtained results can be indicative of a chemi-sorption process in the case of AC-PA activated carbon, despite the results obtained from thermodynamic studies. Nevertheless, in the case of the AC-CA the adsorption could be a physic-sorption process.

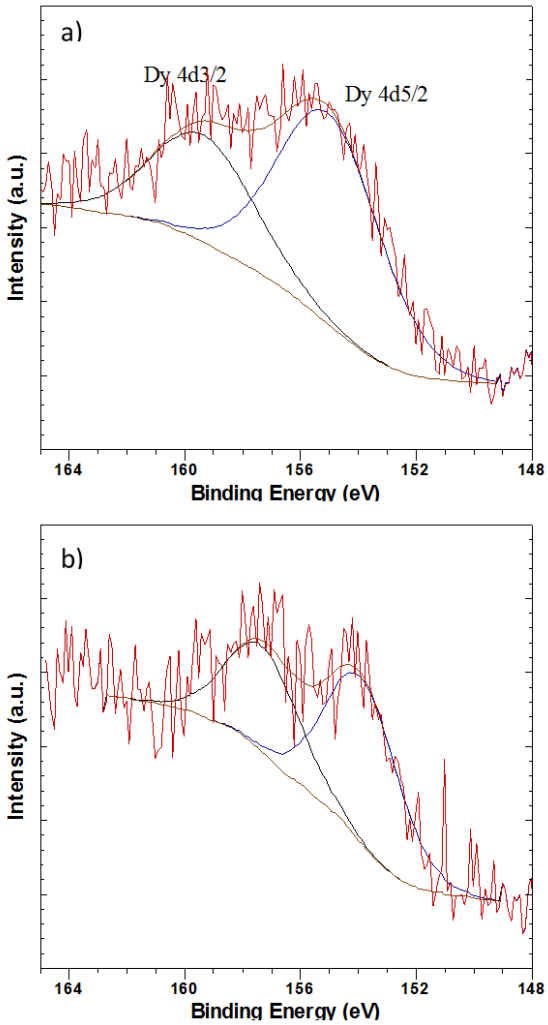

Figure 9. XPS deconvolution spectra of Dy 4d peak of (**a)** AC-PA:Dy and (**b**) AC-CA:Dy

3.4. Photoluminescence spectroscopy (PL)

As most RE, dysprosium cations have s strong visible luminescent emission related to different intraionic transitions [31]. Luminescence spectra of Dy^{3+} active ions are composed of three characteristic bands centered at 480, 575 and 664 nm. These emissions can be attributed to $^4F_{9/2}$-$^6H_{15/2}$, $^4F_{9/2}$-$^6H_{13/2}$ and $^4F_{9/2}$-$^6H_{11/2}$ transitions, respectively [32], among them, the two first are the dominant

components in the spectra [33]. The emission intensity of Dy^{3+} ions may strongly depend on the host matrix, that may significantly influence the radiative and non-radiative properties (multiphonon relaxation as well as energy transfer) leading to different luminescent behavior [32]. Among the different emissions mentioned above, the $^4F_{9/2}$-$^6H_{13/2}$ transition is the most sensitive and the $^4F_{9/2}$-$^6H_{15/2}$ transition is the less sensitive to the matrix [34].

The spectrum shown in Fig. 10 corresponds to the AC-PA:Dy samples. The spectrum exhibits a dominant band peaked at 572 nm and a less intense band centered at around 478 nm. These bands can be attributed to $^4F_{9/2}$-$^6H_{13/2}$ and $^4F_{9/2}$-$^6H_{15/2}$ transitions, respectively. No PL emission could be detected from the AC-CA:Dy samples. Since, in the AC-PA:Dy samples the dominant band is the $^4F_{9/2}$-$^6H_{13/2}$, sometimes referred as hypersensitive transition due to the high sensitivity to the host, structural differences between both types of carbons, could be behind the quenching of the luminescence observed in the AC-CA samples.

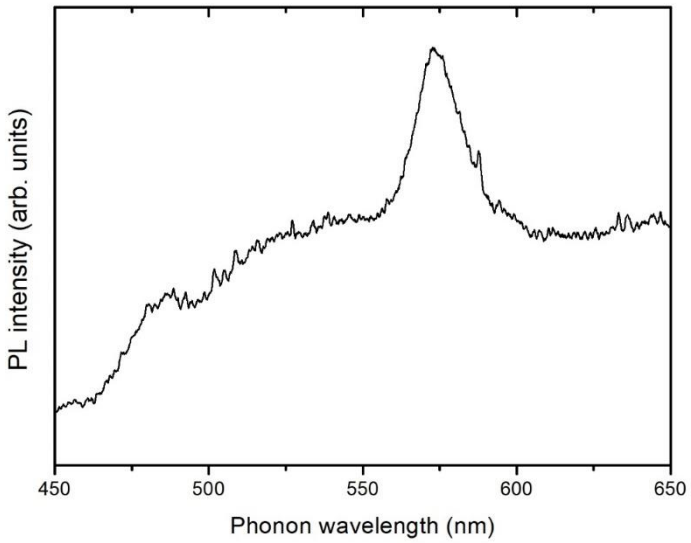

Figure 10. PL spectrum of adsorbed dysprosium onto the AC-PA activated carbon.

5. Conclusions

Dysprosium adsorption experiments exhibit that the variation of the solution pH realizes a great influence in the process, obtaining the maximum adsorption at pH 4. As an expected, a decreases of the solution Dy concentration increases the adsorption percentage. In addition, in the case of chemically activated carbon, the Dy absorbed amount gradually increases with the adsorbent dosage. This effect is not observed in the, where with the exception of the lowest amount used, the adsorption percentage remains practically constant. Finally, the variation of the temperature slightly improves the adsorption process. Despite of this, physically activated carbon exhibits a great adsorption capacity, in all cases. The adsorption isotherms and the kinetic study were better fit with Langmuir model and pseudo-second-order kinetics, respectively, for both investigated activated carbons. So, dysprosium adsorption onto both activated carbons is an exothermic, spontaneous and favorable process as indicate the obtained thermodynamic results. XPS measurements indicate that Dy ions remains in the +3 oxidation state after the adsorption process. Moreover, in the case of the AC-PA:Dy sample, a significant shift to higher binding energies was found indicating higher interaction between Dy ions and the AC. PL spectrum of the Dy loaded AC-PA sample exhibit an emission intensity

centered at 572 nm attributed to the Dy^{3+} ions. So, in the case of the AC-PA activated carbon the Dy adsorption could be a chemi-sorption process.

Nomenclature:

C_0 ($mg \cdot L^{-1}$) = initial concentrations of the RE in solution

C_e ($mg \cdot L^{-1}$) = equilibrium concentrations of the RE in solution

q_t ($mg \cdot g^{-1}$) = adsorption capacity at each time t

V (L) = volume of the solution

m (g) = mass of the activated carbon

q_e ($mg \cdot g^{-1}$) = RE adsorbed amount by mass of the AC at the equilibrium

q_m ($mg \cdot g^{-1}$) = maximum adsorption capacity of the adsorbent per unit mass of adsorbate

b ($L \cdot mg^{-1}$) = Langmuir constant

K_F ($L \cdot g^{-1}$) = Freundlich constant

1/n (adimensional) = adsorption intensity

A_T ($L \cdot g^{-1}$) = Temkin isotherm equilibrium binding constant

T (K) = absolute temperature

B ($J \cdot mol^{-1}$) = ((R·T)/b_T)

b_T = Temkin isotherm constant

R ($kJ \cdot K^{-1} \cdot mol^{-1}$) = universal gas constant

R_L (adimensional) = Langmuir constant or equilibrium parameter. This parameter indicates if the isotherm is reversible (RL=0), favorable (0<RL<1), lineal (RL=1) or unfavorable (RL>1) where RL=1/(1+b·Co)

k_1 (min^{-1}) = pseudo-first-order adsorption constant

k_2 (g·mg-1·min-1) = pseudo-second-order adsorption constant

A ($g \cdot mg^{-1} \cdot min^{-1}$) = temperature-independent factor

ΔH^0 ($kJ \cdot mol^{-1}$) = standard enthalpy change

ΔS^0 ($J \cdot mol^{-1} \cdot K^{-1}$) = standard entropy change

ΔS^0 ($J \cdot mol^{-1} \cdot K^{-1}$) = standard Gibbs free energy

V_T = total pore volume

$V_{\mu p}$ = micropore volume

D_p = average micropore diameter (BJH desorption)

$S_{\mu s}$= microporous surface

$NS_{\mu s}$= non-microporous surface

Author Contributions: L.A. methodology, formal analysis tests, writing original draft preparation; M.E.E. formal analysis; F.J.A. conceptualization and methodology; I.LL. formal analysis; A.U. formal analysis; P.F. formal analysis; writing-review; F.A.L. conceptualization and methodology, supervision, writing-review and editing

Funding: This project has received funding from the European Union's Horizon 2020 research and innovation program under grant agreement No 776851 (carEService)

Acknowledgments: This work has been carried out within the activities of the Card E-Service project.

Conflicts of Interest: The authors declare no conflict of interest.

References

1. Binnemans, K.; Jones, P.T.; Blanpain, B.; Van Gerven, T.; Yang, Y.; Walton, A.; Buchert, M. Recycling of rare earths: A critical review. J. Clean. Prod. 2013, 51, 1–22.
2. Gradin, K.T.; Poulikidou, S.; Björklund, A.; Luttropp, C. Scrutinising the electric vehicle material backpack. J. Clean. Prod. 2018, 172, 1699–1710.
3. Balaram, V. Rare earth elements: A review of applications, occurrence, exploration, analysis, recycling, and environmental impact. Geosci. Front. 2019.
4. Alonso, E.; Sherman, A.M.; Wallington, T.J.; Everson, M.P.; Field, F.R.; Roth, R.; Kirchain, R.E. Evaluating Rare Earth Element Availability: A Case with Revolutionary Demand from Clean Technologies. Environ. Sci. Technol. 2012, 46, 3406–3414.
5. González, A.G.; Pokrovsky, O.S.; Santana-Casiano, J.M.; González-Dávila, M. Bioadsorption of heavy metals. Prospect. Challenges Algal Biotechnol. 2017, 4, 233–255.
6. Fu, F.; Wang, Q. Removal of heavy metal ions from wastewaters: A review. J. Environ. Manage. 2011, 92, 407–418.
7. De Gisi, S.; Lofrano, G.; Grassi, M.; Notarnicola, M. Characteristics and adsorption capacities of low-cost sorbents for wastewater treatment: A review. Sustain. Mater. Technol. 2016, 9, 10–40.
8. Tahir, W.; Choudhry, S. Production of activated carbon from tea waste and its application in water treatment. J. Bio. Env. Sci 2017, 11, 37–44.
9. Malhotra, M.; Suresh, S.; Garg, A. Tea waste derived activated carbon for the adsorption of sodium diclofenac from wastewater: adsorbent characteristics, adsorption isotherms, kinetics, and thermodynamics. Environ. Sci. Pollut. Res. 2018, 25, 32210–32220.
10. S., S.; P., S.K. Influence of ultrasonic waves on preparation of active carbon from coffee waste for the reclamation of effluents containing Cr(VI) ions. J. Ind. Eng. Chem. 2018, 60, 418–430.
11. Laksaci, H.; Khelifi, A.; Trari, M.; Addoun, A. Synthesis and characterization of microporous activated carbon from coffee grounds using potassium hydroxides. J. Clean. Prod. 2017, 147, 254–262.
12. Alcaraz, L.; López Fernández, A.; García-Díaz, I.; López, F.A. Preparation and characterization of activated carbons from winemaking wastes and their adsorption of methylene blue. Adsorpt. Sci. Technol. 2018, 36, 1331–1351.
13. Alguacil, F.; Alcaraz, L.; García-Díaz, I.; López, F. Removal of Pb^{2+} in Wastewater via Adsorption onto an Activated Carbon Produced from Winemaking Waste. Metals (Basel). 2018, 8, 697.
14. Bohli, T.; Ouederni, A.; Fiol, N.; Villaescusa, I. Evaluation of an activated carbon from olive stones used as an adsorbent for heavy metal removal from aqueous phases. Comptes Rendus Chim. 2015, 18, 88–99.
15. Alslaibi, T.M.; Abustan, I.; Ahmad, M.A.; Abu Foul, A. Preparation of Activated Carbon from Olive Stone Waste: Optimization Study on the Removal of Cu^{2+}, Cd^{2+}, Ni^{2+}, Pb^{2+}, Fe^{2+}, and Zn^{2+} from Aqueous Solution Using Response Surface Methodology. J. Dispers. Sci. Technol. 2014, 35, 913–925.
16. Aljeboree, A.M.; Alshirifi, A.N.; Alkaim, A.F. Kinetics and equilibrium study for the adsorption of textile dyes on coconut shell activated carbon. Arab. J. Chem. 2017, 10, S3381–S3393.
17. S. Lagergren Zur Theorie der sogenannten Adsorption gelöster Stoffe. Handlingar 1898, 24, 1–39.
18. Ho, Y..; McKay, G. Pseudo-second order model for sorption processes. Process Biochem. 1999, 34, 451–465.
19. Fouodjouo, M.; Fotouo-Nkaffo, H.; Laminsi, S.; Cassini, F.A.; de Brito-Benetoli, L.O.; Debacher, N.A. Adsorption of copper (II) onto cameroonian clay modified by non-thermal plasma: Characterization, chemical equilibrium and thermodynamic studies. Appl. Clay Sci. 2017, 142, 136–144.
20. Sing, K.S.W. Reporting physisorption data for gas/solid systems with special reference to the determination of surface area and porosity (Recommendations 1984). Pure Appl. Chem. 1985, 57, 603–619.
21. Williams, P.T.; Reed, A.R. Development of activated carbon pore structure via physical and chemical activation of biomass fibre waste. Biomass and Bioenergy 2006, 30, 144–152.
22. Shimodaira, N.; Masui, A.; Takada, A.; Tomita, N. Structural Information from the Raman Spectra of Activated Carbon Materials. Carbon N. Y. 2000.
23. Sfyris, D.; Sfyris, G.I.; Galiotis, C. Stress intrepretation of graphene E-2g and A-1g vibrational modes: theoretical analysis. 2017, 1–30.
24. Wei, Z.; Pan, R.; Hou, Y.; Yang, Y.; Liu, Y. Graphene-supported Pd catalyst for highly selective hydrogenation of resorcinol to 1, 3-cyclohexanedione through giant π-conjugate interactions. Sci. Rep. 2015, 5, 1–9.

25. Ettehadi Gargari, J.; Sid Kalal, H.; Shakeri, A.; Khanchi, A. Synthesis and characterization of Silica/polyvinyl imidazole/H2PO4-core-shell nanoparticles as recyclable adsorbent for efficient scavenging of Sm(III) and Dy(III) from water. J. Colloid Interface Sci. 2017, 505, 745–755.
26. Qadeer, R.; Hanif, J. Adsorption of dysprosium ions on activated charcoal from aqueous solutions. Carbon N. Y. 1995, 33, 215–220.
27. Boparai, H.K.; Joseph, M.; O'Carroll, D.M. Kinetics and thermodynamics of cadmium ion removal by adsorption onto nano zerovalent iron particles. J. Hazard. Mater. 2011, 186, 458–465.
28. Koochaki-Mohammadpour, S.M.A.; Torab-Mostaedi, M.; Talebizadeh-Rafsanjani, A.; Naderi-Behdani, F. Adsorption Isotherm, Kinetic, Thermodynamic, and Desorption Studies of Lanthanum and Dysprosium on Oxidized Multiwalled Carbon Nanotubes. J. Dispers. Sci. Technol. 2014, 35, 244–254.
29. Ghaedi, M.; Nasab, A.G.; Khodadoust, S.; Sahraei, R.; Daneshfar, A. Characterization of zinc oxide nanorods loaded on activated carbon as cheap and efficient adsorbent for removal of methylene blue. J. Ind. Eng. Chem. 2015, 21, 986–993.
30. Barreca, D.; Gasparotto, A.; Milanov, A.; Tondello, E.; Devi, A.; Fischer, R.A. Nanostructured Dy_2O_3 films: An XPS Investigation. Surf. Sci. Spectra 2007, 14, 52–59.
31. Chemingui, S.; Ferhi, M.; Horchani-Naifer, K.; Férid, M. Synthesis and luminescence characteristics of Dy^{3+} doped $KLa(PO_3)_4$. J. Lumin. 2015, 166, 82–87.
32. Grobelna, B.; Synak, A.; Bojarski, P.; Szczodrowski, K.; Kukliński, B.; Raut, S.; Gryczyński, I. Synthesis and luminescence characteristics of Dy^{3+} ions in silica xerogels doped with $Ln_{2-x}Dy_x(WO_4)_3$. Opt. Mater. (Amst). 2013, 35, 456–461.
33. Alcaraz, L.; Isasi, J.; Díaz-Guerra, C. Influence of the synthesis conditions of $Y_{0.9}Dy_{0.1}VO_4$ and silica-coated $Y_{0.9}Dy_{0.1}VO_4$ nanophosphors on the powder morphology and luminescence emission intensity. J. Nanoparticle Res. 2019, 21, 81.
34. Grobelna, B.; Synak, A.; Bojarski, P. The luminescence properties of dysprosium ions in silica xerogel doped with $Gd_{1.6}Dy_{0.4}(WO_4)_3$. Opt. Appl. 2012, 42, 337–344.